Resonant collisions of electrons with O$_2$ via the lowest-lying $^2\Pi_g$ state of O$_2^-$

Václav Alt [*] and Karel Houfek [†]

Institute of Theoretical Physics, Faculty of Mathematics and Physics, Charles University, V Holešovičkách 2, 180 00 Praha 8, Czech Republic

We report the results of an *ab initio* study of resonant vibrational excitation of molecular oxygen by electron impact at low energies where the lowest-lying $^2\Pi_g$ resonant state of O$_2^-$ dominantly contributes to the cross sections. The contribution of this resonance to the dissociative electron attachment cross section is also determined and the origin of its unusual oscillations is discussed. Calculations were performed within the nonlocal resonance model describing the nuclear dynamics of O$_2^-$ after electron capture into the resonant state. The model was constructed using potential-energy curves obtained with standard quantum-chemical methods and eigenphase sums from the fixed-nuclei R-matrix calculations of electron scattering off O$_2$. The effect of the spin-orbit interaction is taken into account when determining the potential-energy curves of the molecular negative ion. The vibrational excitation cross sections are compared with other available theoretical and experimental results.
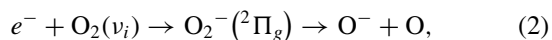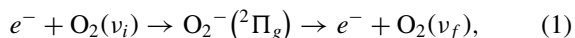
I. INTRODUCTION

The knowledge of accurate cross sections of various processes involving molecular oxygen is important in a range of fields, including physics and chemistry of the Earth's atmosphere [1], where oxygen is the second most abundant molecule, or various models concerning astrophysical plasma or radiation damage [2,3].

Many experimental and theoretical studies have been published about processes involving low-energy electrons and molecular oxygen; see, e.g., the review of the cross sections by Itikawa [4] and references therein. Below we mention only works directly related to our study.

Our interest primarily lies in resonant collisions of electrons with O$_2$ resulting in vibrational excitation (VE) and dissociative electron attachment (DA):

$$e^- + O_2(\nu_i) \rightarrow O_2^-(^2\Pi_g) \rightarrow e^- + O_2(\nu_f), \quad (1)$$

$$e^- + O_2(\nu_i) \rightarrow O_2^-(^2\Pi_g) \rightarrow O^- + O, \quad (2)$$

where ν_i and ν_f are initial and final vibrational states, respectively. Although another process of rotational excitation plays an important role at low energies, we do not consider it in this paper and we also neglect any rotational effects for the process (1) because these effects are very small for oxygen at low temperatures. However, they can be significant for dissociative attachment (2) as the threshold decreases for higher initial rotational states. Since we are primarily interested in the interpretation of the structures appearing in the DA cross sections and not in providing data to be directly compared with experiments, we do not study this process for higher rotational states.

At energies from 0 to 2.5 eV, the dynamics of these collisions dominantly proceeds via the lowest-lying resonant electronic $^2\Pi_g$ state of O$_2^-$. This resonance manifests itself in the form of sharp peaks in the VE cross sections, each peak corresponding to a vibrational level of the negative ion. These peaks were first observed in the early measurements of Boness and Schulz [5] and of Linder and Schmidt [6] in the differential cross sections, and later by Land and Raith [7] in the total cross sections. More recent measurements by Field *et al.* [8] and by Allan [9] show a great improvement in resolution allowing the observation of the spin-orbit splitting of the $^2\Pi_g$ resonant state. The most recent work of Okumura [10] presents the absolute total cross section with a striking resolution of 7 meV.

Several theoretical works that considered collisions of electrons with molecular oxygen have been published, but most of them focus only on the fixed-nuclei electron-scattering calculations and not on the nuclear dynamics which is necessary to provide a proper description of the processes (1) and (2). Noble, Burke, *et al.* [11,12] first employed the R-matrix method to obtain the fixed-nuclei scattering cross sections. Afterwards, they calculated the cross sections for several VE transitions [13] using the method developed by Schneider *et al.* [14] getting satisfactory agreement with the experiment by Field *et al.* [8]. Later works [15,16] also applied the R-matrix approach or used a combination of other methods but usually covered larger energies and subsequently needed to treat higher electronic resonances of O$_2^-$. The most recent treatment of the nuclear dynamics for the processes (1) and (2) was provided by Laporta *et al.* [17,18] within the local complex potential (LCP) approximation, also known as the *boomerang model* [19].

Collisions of electrons with many diatomic molecules of interest [20] have been described within the nonlocal resonance model (also known as the discrete-state-in-continuum approach) reviewed by Domcke [21] and by Čížek and Houfek [22]. However, the O$_2$ molecule has not yet been treated

---
[*]vaclav.alt@utf.mff.cuni.cz
[†]houfek@mbox.troja.mff.cuni.cz

within this approach, which proved to be necessary to get the correct behavior of the cross sections near thresholds [23]. In this paper we present the VE and DA cross sections for O_2 obtained within the nonlocal resonance model constructed for the lowest-lying $^2\Pi_g$ resonant state and we compare them with the results of the works cited above.

II. THEORY FOR NUCLEAR DYNAMICS

A. Discrete state in continuum

For the nuclear dynamics involved in the processes (1) and (2) we use the nonlocal resonance model (NRM) [21]. This theory assumes that a metastable state of the incoming electron captured by a molecule can be described by a square-integrable, diabatic discrete state $|\phi_d\rangle$ with the energy $V_d(R)$ dependent on the internuclear distance R. The discrete state interacts with electronic continuum via the coupling element $V_{d\varepsilon}(R)$, which is a function of R and electron energy ε.

The theory is based on the Feshbach projection-operator approach [21,24,25] and leads to the equation for the nuclear wave function $\psi_d(R)$, which corresponds to the discrete-state part of the electronic Hilbert space,

$$[E - T_R - V_d(R)]\psi_d(R) - \int dR' \, F(E, R, R')\psi_d(R')$$
$$= V_{d\varepsilon_{v_i}}(R)\chi_{v_i}(R), \qquad (3)$$

where E is the total energy of the system and

$$T_R = -\frac{1}{2\mu}\frac{\partial^2}{\partial R^2}$$

is the kinetic-energy operator of the relative motion of the nuclei with the reduced mass μ. The interaction with the continuum is effectively described by the nonlocal, complex, and energy-dependent potential

$$F(E, R, R') = \Delta(E, R, R') - \frac{i}{2}\Gamma(E, R, R'). \qquad (4)$$

This potential can be expressed using the expansion into the vibrational states of the neutral molecule as

$$F(E, R, R') = \sum_v \chi_v(R)\left[\tilde{\Delta}(\varepsilon_v, R, R')\right.$$
$$\left. - \frac{i}{2}\tilde{\Gamma}(\varepsilon_v, R, R')\right]\chi_v^*(R'), \qquad (5)$$

where $\varepsilon_v = E - E_v$ is electron energy when the molecule is in the vibrational state $\chi_v(R)$ with the energy E_v. These vibrational states satisfy the equation

$$[T_R + V_0(R)]\chi_v(R) = E_v\chi_v(R), \qquad (6)$$

with $V_0(R)$ being the potential energy of an electronic state of the neutral molecule (in our case the lowest one). The level shift $\tilde{\Delta}(\varepsilon, R, R')$ and the resonance width $\tilde{\Gamma}(\varepsilon, R, R')$ are given by

$$\tilde{\Gamma}(\varepsilon, R, R') = 2\pi V_{d\varepsilon}(R)V_{d\varepsilon}^*(R'), \qquad (7)$$

$$\tilde{\Delta}(\varepsilon, R, R') = \frac{1}{2\pi}\text{P.V.} \int d\varepsilon' \frac{\tilde{\Gamma}(\varepsilon', R, R')}{\varepsilon - \varepsilon'}, \qquad (8)$$

where P.V. denotes the Cauchy principal value.

The cross sections for vibrational excitation $v_i \to v_f$ and for dissociative attachment can be obtained as

$$\sigma_{v_iv_f}(E) = g\frac{4\pi^3}{k_i^2}\left|\int_0^\infty dR \, \chi_{v_f}^*(R)V_{dE_f}(R)\psi_d(R)\right|^2, \qquad (9)$$

$$\sigma_{DA}(E) = g\frac{2\pi^2}{k_i^2}\frac{K}{\mu}\lim_{R \to \infty}|\psi_d(R)|^2, \qquad (10)$$

where g is the statistical factor, k_i is the initial electron momentum corresponding to the energy ε_{v_i}, and K is the relative momentum of the outgoing nuclei in the DA channel with energy $E - V_d(R)|_{R\to\infty} = K^2/2\mu$ (see Refs. [21,23] for more details).

B. Local complex potential approximation

If $V_{d\varepsilon}(R)$ depends weakly on energy then for a fixed internuclear distance R, electron energy ε can be approximated by resonance energy $E_{res}(R)$. From Eqs. (5) and (7) it follows that $\Gamma(E, R, R')$ becomes local and energy independent [26]:

$$\Gamma(E, R, R') \approx 2\pi \sum_v \chi_v(R)\left|V_{dE_{res}(R)}\right|^2 \chi_v^*(R')$$
$$= 2\pi\left|V_{dE_{res}(R)}\right|^2 \delta(R - R'). \qquad (11)$$

Consequently, the energy-independent local resonance width can be defined as

$$\Gamma(R) = 2\pi\left|V_{dE_{res}(R)}\right|^2. \qquad (12)$$

Similarly, $\Delta(E, R, R')$ reduces to

$$\Delta(R) = \frac{1}{2\pi}\text{P.V.}\int dE' \frac{\Gamma(R)}{E_{res}(R) - E'}. \qquad (13)$$

The substitution of Eqs. (12) and (13) into Eq. (3) yields

$$[E - T_R - V_{loc}(R)]\psi_d(R) = \sqrt{\frac{\Gamma(R)}{2\pi}}\chi_{v_i}(R), \qquad (14)$$

with $V_{loc}(R)$ being the local complex potential given by

$$V_{loc}(R) = V_{ion}(R) - \frac{i}{2}\Gamma(R)$$
$$= V_d(R) + \Delta(R) - \frac{i}{2}\Gamma(R). \qquad (15)$$

The VE cross sections are now given by

$$\sigma_{v_iv_f}(E) = g\frac{4\pi^3}{k_i^2}\left|\int dR \, \chi_{v_f}^*(R)\sqrt{\frac{\Gamma(R)}{2\pi}}\psi_d(R)\right|^2. \qquad (16)$$

The DA cross section is still given by Eq. (10).

III. CALCULATION DETAILS

A. Potential-energy curves

The potential-energy curves of the electronic states $^3\Sigma_g^-$ of O_2 and $^2\Pi_g$ of O_2^- with the dominant electronic configurations

$$^3\Sigma_g^- : 1\sigma_g^2 1\sigma_u^2 2\sigma_g^2 2\sigma_u^2 3\sigma_g^2 1\pi_u^4 1\pi_g^2,$$
$$^2\Pi_g : 1\sigma_g^2 1\sigma_u^2 2\sigma_g^2 2\sigma_u^2 3\sigma_g^2 1\pi_u^4 1\pi_g^3,$$

TABLE I. Comparison of calculated electron affinities E_{ea} and dissociation energy D_0 with experimental values. Calc. + shift means that the $^2\Pi_g$ curve was shifted to reproduce experimental $E_{ea}(\text{O})$.

	$E_{ea}(\text{O})$ (eV)	$E_{ea}(\text{O}_2)$ (eV)	$D_0(\text{O}_2)$ (eV)
expt. [33]	1.4611096(7)	0.450(2)	5.165(2)
calc.	1.198	0.211	5.159
calc. + shift	1.461	0.474	5.159

were obtained by employing the complete-active-space self-consistent-field (CASSCF) and multireference configuration-interaction (MRCI) methods. The CASSCF method [27,28] was used to construct natural molecular orbitals by optimizing energies of these states separately for O₂ and O₂⁻. The MRCI calculations [29] followed to improve the relative energy between the $^3\Sigma_g^-$ and $^2\Pi_g$ states. Both calculations were carried out using the MOLPRO quantum chemistry package [30,31] with the aug-cc-pVQZ basis set [32]. The complete active space (CAS) was spanned by molecular orbitals $(3\sigma_g 1\pi_u 1\pi_g 3\sigma_u 4\sigma_g 2\pi_u 2\pi_g 4\sigma_u 5\sigma_g 5\sigma_u)$ with $(1\sigma_g 1\sigma_u 2\sigma_g 2\sigma_u)$ kept closed in both calculations.

The quality of calculated potential-energy curves was assessed by comparing electron affinities E_{ea} and dissociation energy D_0 with available experimental data. Since it is very computationally demanding to converge to the correct electron affinity of the atomic oxygen for large internuclear distances, we decided to adjust the $^2\Pi_g$ curve to reproduce the experimental value 1.461 eV taken from Ref. [33]. If the shapes of the curves were correct then, after this adjustment, one should obtain the correct value of $E_{ea}(\text{O}_2)$. The comparison in Table I shows that the calculated value of $E_{ea}(\text{O}_2)$ is 24 meV higher than the experimental value 0.45 eV. In the end, we decided to use the shifted $^2\Pi_g$ curve to get the correct DA threshold, even though positions of the narrow peaks in the VE cross sections can be slightly misplaced when compared with the experimental ones.

We also performed several larger calculations with the aug-cc-pV5Z and aug-cc-pV6Z basis sets and tried the complete-basis-set extrapolation to obtain more accurate potential-energy curves. However, the relative shape and position of the curves were not improved in comparison with the shifted aug-cc-pVQZ curves and thus we decided to use the results obtained with the smaller basis set.

The splitting of peaks occurring due to the spin-orbit interaction was observed in the experimental VE cross sections [8–10]. To include this phenomenon into our model, we calculated the spin-orbit correction to the $^2\Pi_g$ curve by diagonalizing the spin-orbit matrix in the smaller cc-pVTZ basis set [32] within the MRCI method of the MOLPRO package. The Gaussian fit to these data shown in Fig. 1 was then used to obtain the $^2\Pi_g^{1/2}$ and $^2\Pi_g^{3/2}$ potential-energy curves of O₂⁻ which lie symmetrically around the $^2\Pi_g$ curve. The effect is too small to be visible in Fig. 2 where potential-energy curves of models for nuclear dynamics calculations are shown, but see the detail of the potential curves in Fig. 6. Each of these two curves was used for independent calculation of the nuclear dynamics within both LCP and NRM models.
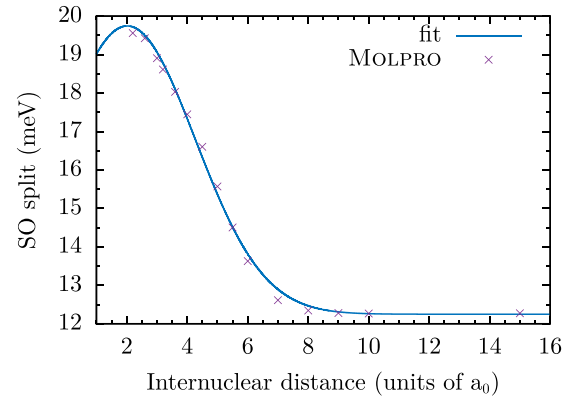

FIG. 1. Dependence of the total spin-orbit (SO) splitting of the $^2\Pi_g$ potential-energy curve of O₂⁻ on the internuclear distance together with its Gaussian fit. Internuclear distances are given in atomic units, i.e., in units of the Bohr radius $a_0 = 5.291\,772 \times 10^{-10}$ m.

B. Fixed-nuclei scattering

The character of the anion $^2\Pi_g$ electronic state depends on the internuclear distance. For large distances, the extra electron is bound and the state is described by the real-valued potential-energy curve discussed in the previous section (bound-state region). However, the anion state crosses the $^3\Sigma_g^-$ state of the neutral molecule close to its equilibrium and becomes metastable for short distances (resonance region). As a result, its potential-energy becomes complex-valued. This complex part of the anion curve was determined from fixed-nuclei scattering data obtained using the R-matrix method [34], as implemented in the UKRmol suite of codes [35,36]. In this approach, the wave function describing the compound system of $N + 1$ electrons in the inner region is expanded into the basis functions of the form

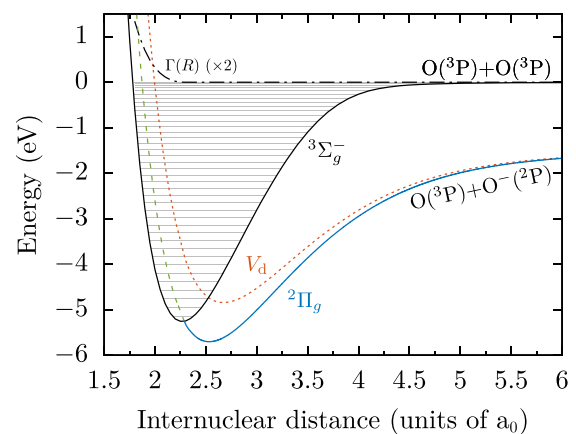$$\Psi_k^{N+1} = \mathcal{A} \sum_{i,j} a_{ijk} \Phi_i^N \gamma_{ij} + \sum_i b_{ik} \chi_i^{N+1}, \qquad (17)$$

FIG. 2. Potential-energy curves of O₂ and O₂⁻ (full lines), the real part of the complex potential energy of the $^2\Pi_g$ state (dashed line), the discrete-state potential V_d of the nonlocal resonance model (dotted line), and the local resonance width $\Gamma(R)$ (dash-dotted line).

where Φ_i^N are the bound electronic states of the neutral molecule (target), γ_{ij} describe the scattered electron, and χ_i^{N+1} are L^2-integrable functions included to describe possible resonant states in the system. The operator $\mathcal{A}$ ensures the proper antisymmetrization.

The target functions Φ_i^N were again obtained by the CASSCF method, but with the smaller cc-pVTZ basis [32]. The general structure of used configuration state functions was

$$\Phi_i^N \; : \; [\text{core}]^{N_c}[\text{CAS}]^{N-N_c}, \tag{18}$$

with the complete active space spanned by $[\text{CAS}] = (2\sigma_g 2\sigma_u 3\sigma_g 1\pi_u 1\pi_g 3\sigma_u)$ orbitals and with $[\text{core}] = (1\sigma_g 1\sigma_u)$ orbitals kept frozen. The L^2-functions χ_i^{N+1} were chosen according to the overall symmetry in the general forms

$$\chi_i^{N+1} : [\text{core}]^{N_c}[\text{CAS}]^{N-N_c+1},$$
$$\text{and } [\text{core}]^{N_c}[\text{CAS}]^{N-N_c}[\text{virtual}]^1. \tag{19}$$

The resonance energy $E_{\text{res}}(R)$ and width $\Gamma(R)$ can be extracted from the eigenphase sums $\delta_{\text{sum}}(\varepsilon, R)$ produced by the R-matrix scattering calculations. Within the UKRmol suite this is achieved with the program RESON [37] by fitting the Breit-Wigner formula to the K matrices:

$$K(\varepsilon, R) = \tan \delta_{\text{sum}}(\varepsilon, R) = \frac{\frac{1}{2}\Gamma(R)}{E_{\text{res}}(R) - \varepsilon}. \tag{20}$$

The real part of the anion curve in the resonance region is constructed as

$$V_{\text{ion}}(R) = V_0(R) + E_{\text{res}}(R). \tag{21}$$

We varied the R-matrix scattering models by changing the number of bound states Φ_i^N in Eq. (17) and the number of virtual orbitals in Eq. (19). We found several models which produced a satisfactory continuation of the $^2\Pi_g$ curve to the bound-state region. Eventually, we decided to use the R-matrix model with three lowest target states and ten virtual orbitals to construct both the nonlocal and local models for nuclear dynamics, since it gives the smoothest continuation of the $^2\Pi_g$ curve from MOLPRO calculations. The final potential-energy curves are depicted in Fig. 2.

C. Nonlocal resonance model

The nonlocal resonance model was constructed by fitting the generalized Breit-Wigner formula (23) to the eigenphase sums obtained in the R-matrix calculations. We suppose the eigenphase sums can be expressed as

$$\delta(\varepsilon, R) = \delta_{\text{bg}}(\varepsilon, R) + \delta_{\text{res}}(\varepsilon, R), \tag{22}$$

$$\delta_{\text{res}}(\varepsilon, R) = -\arctan\left(\frac{\frac{1}{2}\tilde{\Gamma}(\varepsilon, R)}{\varepsilon - V_{\text{d}}(R) - \tilde{\Delta}(\varepsilon, R) + V_0(R)}\right), \tag{23}$$

where δ_{bg} is assumed to take the simple form

$$\delta_{\text{bg}}(\varepsilon, R) = c\varepsilon^\alpha, \tag{24}$$

TABLE II. Nonlocal resonance model parameters in atomic units (a_0 is the Bohr radius, E_{h} is the Hartree energy).

a_0	13.836690	$E_{\text{h}}^{-1.5}$	b_0	3.015014	$E_{\text{h}}^{-1.5}$
a_1	0.892095	$E_{\text{h}}^{-1.5}a_0^{-1}$	b_1	0.718160	$E_{\text{h}}^{-1.5}a_0^{-1}$
a_2	−0.935987	a_0^{-1}	c	−14.260279	$E_{\text{h}}^{-2.5}$

with $\alpha = l + 1/2$ and $l = 2$ for the $^2\Pi_g$ resonance of O_2^-. We used the following form of the width function:

$$\tilde{\Gamma}(\varepsilon, R) = 2\pi \varepsilon^\alpha A(R) \exp^{-B(R)\varepsilon}, \tag{25}$$

where

$$A(R) = (a_0 + a_1 R) \exp(a_2 R), \tag{26}$$

$$B(R) = b_0 + b_1 R, \tag{27}$$

since it allows us to evaluate the level-shift function

$$\tilde{\Delta}(\varepsilon, R) = \frac{1}{2\pi} \text{P.V.} \int d\varepsilon' \frac{\tilde{\Gamma}(\varepsilon', R)}{\varepsilon - \varepsilon'} \tag{28}$$

in closed form [21]. To construct the discrete-state potential $V_{\text{d}}(R)$ we used the resonance energy $E_{\text{res}}(R)$ from the R-matrix calculations. Thus, $V_{\text{d}}(R)$ is given by

$$V_{\text{d}}(R) = V_0(R) + E_{\text{res}}(R) - \tilde{\Delta}(E_{\text{res}}(R), R). \tag{29}$$

The nonlocal functions $\tilde{\Delta}(\varepsilon, R, R')$ and $\tilde{\Gamma}(\varepsilon, R, R')$ were constructed from their local versions as follows:

$$\tilde{\Gamma}(\varepsilon, R, R') = \sqrt{\tilde{\Gamma}(\varepsilon, R)\tilde{\Gamma}(\varepsilon, R')}, \tag{30}$$

$$\tilde{\Delta}(\varepsilon, R, R') = \frac{1}{2\pi} \text{P.V.} \int d\varepsilon' \frac{\tilde{\Gamma}(\varepsilon, R, R')}{\varepsilon - \varepsilon'}. \tag{31}$$

Equation (3) was then solved by employing methods described in Refs. [38,39].

The unknown parameters in Eqs. (24), (26), and (27) were determined with the Nelder-Mead algorithm (also known as Amoeba) [40] by minimizing the mean-squared error of the eigenphase sums using the shifted potential-energy curves to match the experimental electron affinity of the oxygen atom (see Table I). The final values are listed in Table II. For several internuclear distances R, the eigenphase sums are plotted in Fig. 3 and the local width $\tilde{\Gamma}(\varepsilon, R)$ and level shift $\tilde{\Delta}(\varepsilon, R)$ in Fig. 4.

If the $^2\Pi_g$ resonance of O_2^- is treated without spin-orbit splitting, the statistical factor g in the cross sections would be [41]

$$g(^2\Pi_g) = \tfrac{2}{3}.$$

When the spin-orbit separation is considered, the factors become

$$g(^2\Pi_g^{1/2}) = g(^2\Pi_g^{3/2}) = \tfrac{1}{3}.$$

Because the cross section for both $^2\Pi_g^{1/2}$ and $^2\Pi_g^{3/2}$ states are calculated separately, the final VE or DA cross sections are their sum

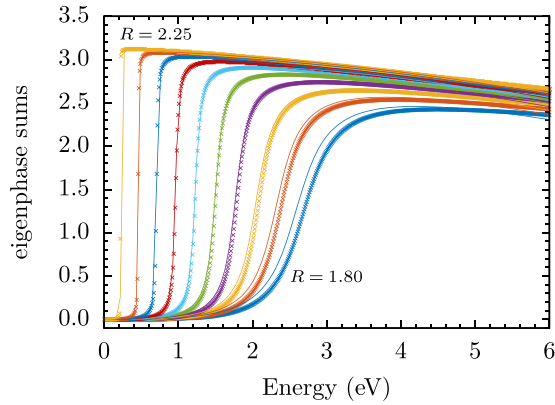$$\sigma(E) = \sigma_{^2\Pi_g^{1/2}}(E) + \sigma_{^2\Pi_g^{3/2}}(E).$$

FIG. 3. Eigenphase sums from the R-matrix scattering calculations (points) and the fitted curves (lines) obtained when constructing the nonlocal resonance model. From right to left, the curves correspond to internuclear distances of 1.80, 1.85, 1.90, 1.95, 2.00, 2.05, 2.10, 2.15, 2.20, and 2.25 in units of a_0.

IV. RESULTS

A. Vibrational excitation

The cross sections for vibrational excitation of the O_2 molecule in its ground vibrational state calculated using the nonlocal resonance model and the local complex potential approximation are shown in Fig. 5. Double peaks, appearing in all cross sections at the same positions, correspond to the vibrational levels in the real part of the $^2\Pi_g^{1/2}$ and $^2\Pi_g^{3/2}$ potential-energy curves of O_2^- as one can clearly observe in Fig. 6 for several VE cross sections.

The LCP results for inelastic transitions are much larger at low energies, as one can expect due to the incorrect threshold behavior of the local width $\Gamma(R)$, which is energy-dependent in the nonlocal approach. Especially in the $0 \to 2$ cross sections, the peak stemming from vibrational level $\nu' = 7$ of O_2^- at around 0.46 eV is not visible at all in the NRM cross section. However, it is still present but strongly suppressed.
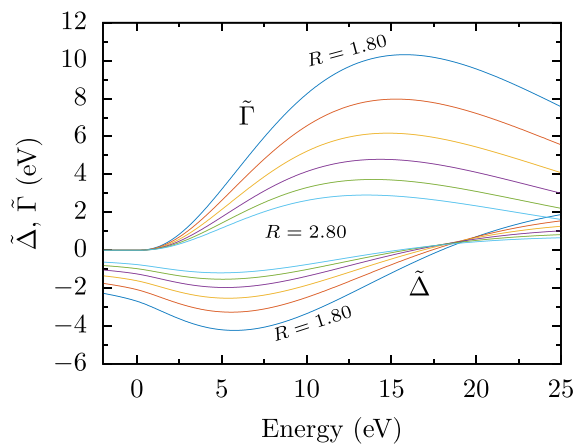

FIG. 4. Local width $\tilde{\Gamma}(\varepsilon, R)$ and level shift $\tilde{\Delta}(\varepsilon, R)$ as functions of electron energy and internuclear distance. The curves correspond to internuclear distances of 1.80, 2.00, 2.20, 2.40, 2.60, and 2.80 in units of a_0, the closer a curve is to the zero energy, the larger the internuclear distance.

In Fig. 7 we compare the VE cross sections obtained within the nonlocal model without the spin-orbit splitting with the results of Higgins *et al.* [13], which were retrieved by digitizing graphs presented therein. The first peak at 0.1 eV in the elastic channel was cut short by the graph range, and therefore, it appears to be much lower. However, Higgins *et al.* mention that the height of the first peak exceeds $1200a_0^2$. The heights of the other peaks are in a reasonable agreement with our results, with the exception of the peak at 0.8 eV of the $0 \to 3$ excitation, which is suppressed in our model. All peaks in the results of Higgins *et al.* are uniformly shifted towards higher energies by approximately 20 meV (the value comparable to the spin-orbit splitting). Since the position of the peaks clearly corresponds to the vibrational levels of O_2^-, this shift is most likely caused by the difference in the relative position of the potential-energy curves of the $^3\Sigma_g^-$ and $^2\Pi_g$ states. Moreover, there is also a notable difference in widths of the individual peaks. In our results, the widths of the peaks are approximately four times smaller than those of Higgins *et al.* Table III shows relative intensities of several peaks in the total cross section compared with results of Higgins *et al.* and of Field *et al.* [8] (discussed later). Our total cross sections are obtained as the sum of all calculated VE cross sections. We calculated the intensities as integrals over individual peaks, Higgins *et al.* approximated them by rectangles. Relative intensities of peaks corresponding to vibrational levels $\nu' = 4$–6 agree quite well despite rather large discrepancy in the peak widths. For $\nu' = 8, 9$, Higgins *et al.* claim that the rectangle approximation starts to fail, which causes disagreement with results of Field *et al.*

To compare our results with experimental ones we convolved our data using the general formula

$$\sigma_c(\varepsilon) = \int d\varepsilon' \sigma(\varepsilon') g(\varepsilon - \varepsilon', \sigma_{FWHM}), \qquad (32)$$

where $\sigma(\varepsilon)$ is a certain calculated VE cross section and $g(\varepsilon, \sigma_{FWHM})$ is the normalized Gaussian distribution simulating the finite experimental resolution. The effect of the convolution for the VE $0 \to 1$ cross section as calculated within the nonlocal resonance model is illustrated in Fig. 8.

The experimental VE cross sections of Allan [9] were measured with the finite-energy resolution of $\sigma_{FWHM} = 10$ meV for transitions $0 \to 1$–3 and $\sigma_{FWHM} = 15$ meV for $0 \to 4$–7. In Fig. 9 we compare these experimental results with the convolved VE cross sections calculated using the LCP approximation (upper panel) and the NRM (lower panel). Since Allan presented his data in arbitrary units, we normalized our cross sections to get the same maximal value of the highest peaks. All calculated peaks are shifted to higher energies by around 10 meV, which is still well within the 30 meV experimental uncertainty [9]. Furthermore, Allan explicitly measures spin-orbit separation in the $0 \to 1$ cross section on the $\nu' = 9$ doublet as 19.6 ± 1.0 meV. Our calculation shows the separation of 17.8 meV. The discrepancy of 1.8 meV is still much less then the typical errors of the quantum-chemistry calculations [42] and we consider the agreement to be very good.

We can see that neither the local nor the nonlocal approach are able to accurately reproduce the experimental relative
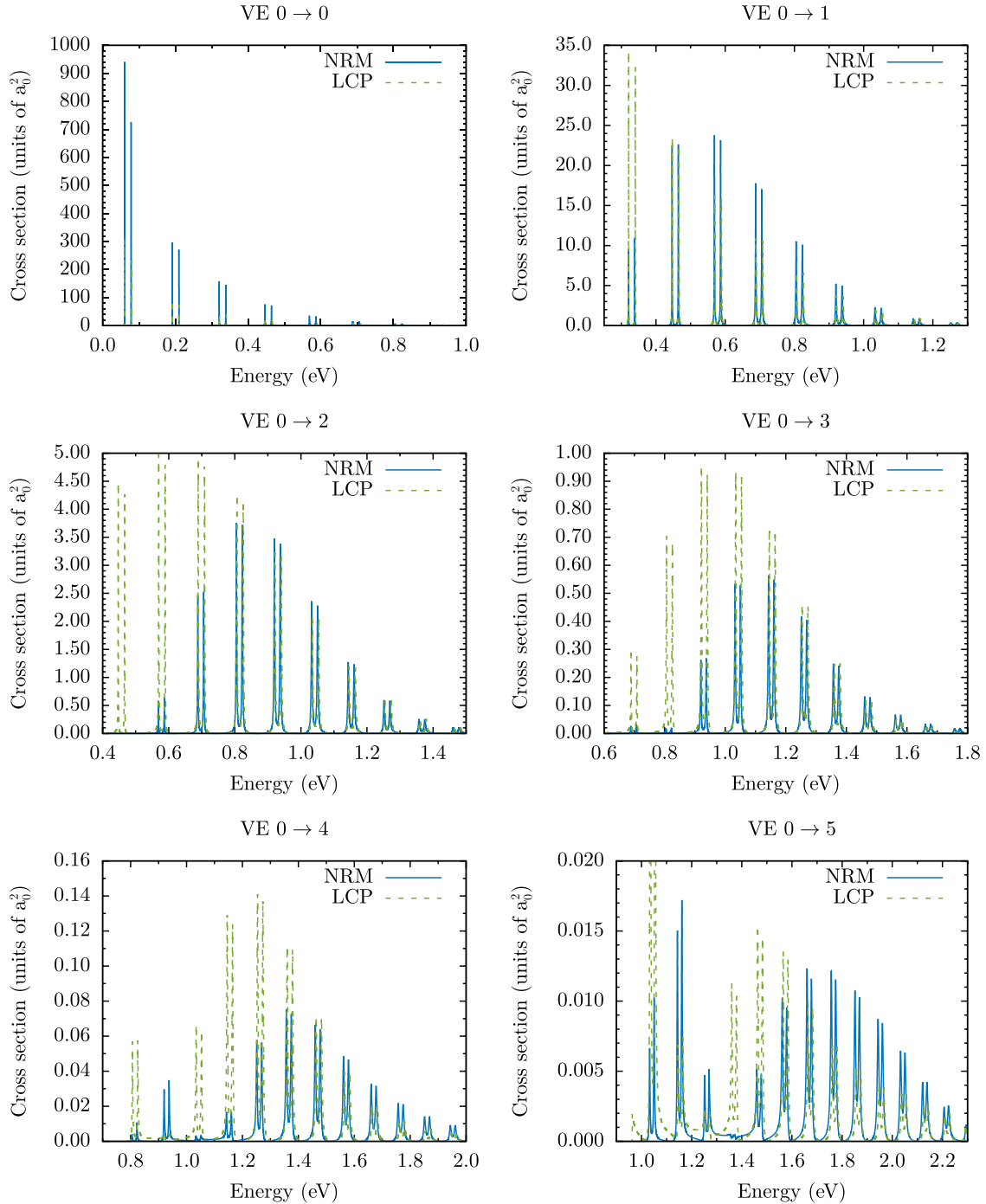
FIG. 5. Comparison of the vibrational excitation cross sections from $\nu_i = 0$ to $\nu_f = 0$–6 calculated within the nonlocal resonance model (NRM) and the local complex potential (LCP) approximation.

heights of the individual peaks. The local approximation (LCP) tends to amplify peaks on the low-energy side because of its incorrect threshold behavior. Our nonlocal resonance model on the other hand seems to suppress these peaks too much. There are also significant discrepancies at higher energies for transitions $0 \rightarrow 5$–7 in both approaches.

Figure 10 displays the resonant contribution to the total cross section obtained within the nonlocal resonant model compared with the results of Field *et al.* [8] who measured the total cross sections with energy resolution of 3.5 meV. In Fig. 10, we only show the convolutions of our NRM results

with σ_{FWHM} of 7 and 15 meV. The convolution with $\sigma_{FWHM} = 3.5$ meV produces peaks much higher than those of Field *et al.* In comparison with Higgins *et al.*, our cross sections show narrower and higher peaks, but the relative intensities remain roughly the same, see Table III. There seems to be a disproportionate difference in the peak heights at 0.2 eV. Field *et al.* obtained the resonant part of the cross sections by subtraction of the nonresonant part from the total cross sections, which may introduce inaccuracies, especially when the resonant contribution is small compared with the nonresonant part. Field *et al.* also observed the spin-orbit splitting of the
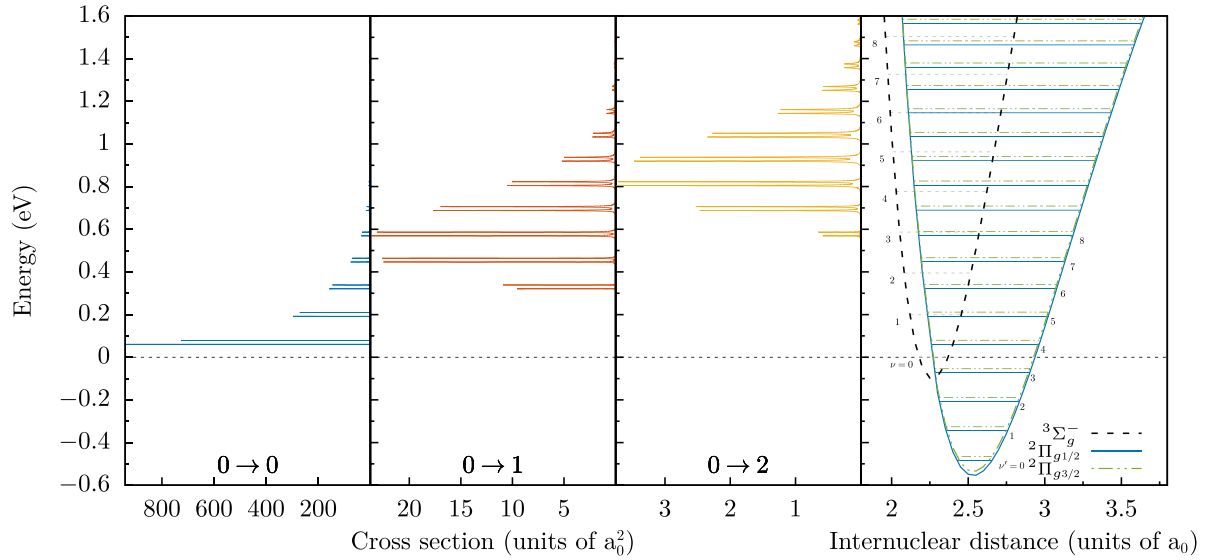
FIG. 6. Sharp peaks in the different VE cross sections lie always at the same positions, clearly corresponding to the quasibound vibrational levels of O_2^-.

$^2\Pi_g$ resonance and measured the magnitude of the split to be 18.8 ± 1.0 meV, which is again in a very good agreement with our result.

In Fig. 11, we compare the resonant contribution to the total cross section with the resonant component of the absolute total cross section for electron scattering from O_2 measured by Okumura *et al.* [10] with the resolution of 7 meV. Therefore, the calculated cross sections were convolved with $\sigma_{\text{FWHM}} =$

7 meV. Our NRM results are 2–5 times larger depending on the peak. The positions of the peaks agree well at higher energies. However, there is a significant shift of the peaks at lower energies reaching approximately 22 meV for the first peak, the value which is larger than the spin-orbit separation. This may be caused by inaccuracies in the potential-energy curves. Our value of $E_{ea}(O_2)$ is larger by 24 meV than the experimental value, see Table I, which is very close to the discrepancy of
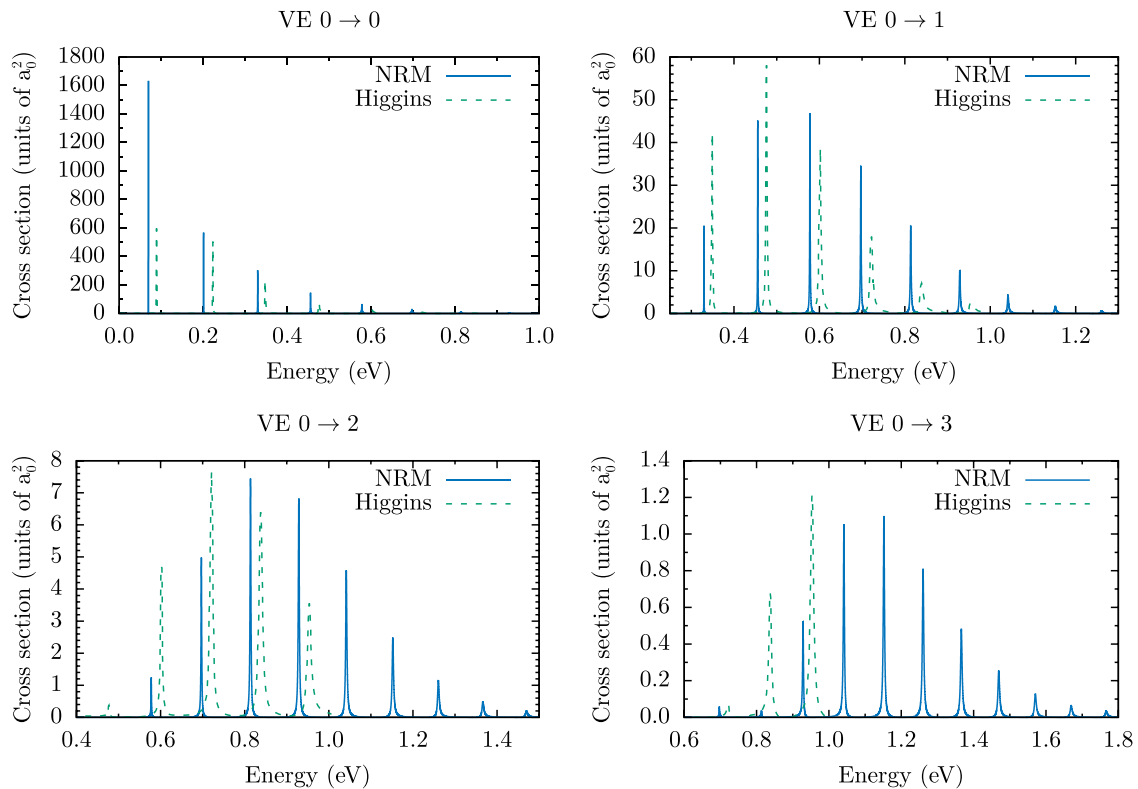

FIG. 7. Vibrational excitation cross sections obtained within the nonlocal resonance model without the spin-orbit splitting of the $^2\Pi_g$ state compared with the results of Higgins *et al.* [13] who published the cross sections only up to 1 eV.

TABLE III. Relative peak intensities in the total cross section. The experiment and theory are normalized to 1 for $\nu' = 7$.

ν'	Field [8]	Higgins [13]	LCP	NRM
4		0.227	1.008	0.141
5	0.63	0.664	0.522	0.542
6	0.86	0.875	0.879	0.852
7	1.00	1.000	1.000	1.000
8	0.91	0.751	1.031	0.989
9	0.64	0.520	0.951	0.837

22 meV observed here. Small variations of potential-energy curves can, however, cause significant changes in positions and spacing of the peaks in the cross sections.

Applications use the rate coefficients for VE processes defined as

$$k_{\nu_i \nu_f}(T) = \sqrt{\frac{8}{m_e \pi}} \left(\frac{1}{T_e}\right)^{3/2} \int_0^\infty dE \, E \sigma_{\nu_i \nu_f}(E) e^{-E/T_e}, \quad (33)$$

where we assume the Maxwell-Boltzmann electron energy distribution at temperature T_e given in electronvolts. The rate coefficients at very low temperatures can be sensitive to the model used for the cross-section calculations. We illustrate this sensitivity in Fig. 12, where we show the rate coefficients for two VE transitions $0 \to 0$ and $0 \to 2$. Since our study focuses on the lowest-lying $^2\Pi_g$ resonance, we show the results only up to 2.0 eV, because other resonances start to contribute significantly at higher energies. The rate coefficients can differ by a factor 2–5 not only when comparing the NRM and LCP models but also when comparing our LCP results with those of Laporta *et al.* [17], which were also calculated within the LCP model with slightly different potential-energy curves.

B. Dissociative attachment

The contribution of the $^2\Pi_g$ resonance to the DA cross section for O_2 in its ground vibrational state as calculated within our NRM and LCP models is shown in Fig. 13. We encountered the same oscillatory behavior of the cross section
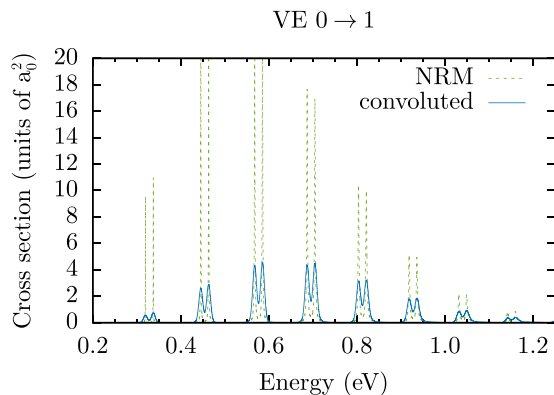

FIG. 8. NRM cross section for vibrational excitation $0 \to 1$ before and after convolution with the Gaussian distribution for $\sigma_{\text{FWHM}} = 10$ meV, the experimental resolution of Allan [9] for this particular process.
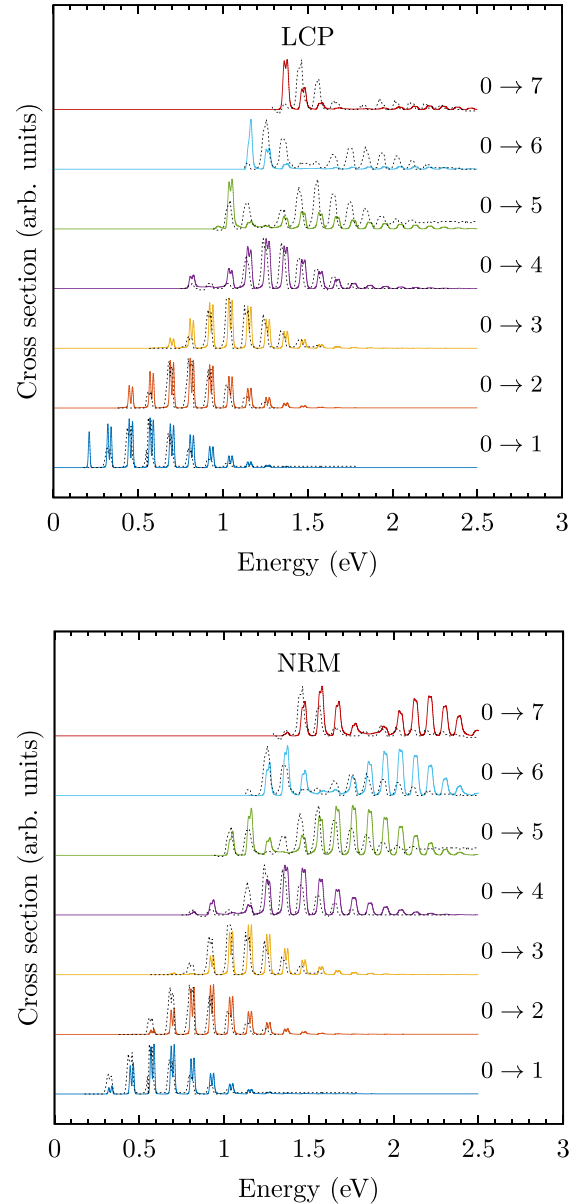

FIG. 9. Vibrational excitation cross sections (solid lines) obtained within the local approximation (upper panel) and the nonlocal model (lower panel), convolved using the experimental resolution, compared with the data of Allan (dashed lines) [9]. Each cross section is normalized to get the same maximum of the highest peak.

as Laporta *et al.* [18], but their cross section is approximately 100 times larger. Because the DA cross section at the threshold is quite small, such a large disagreement can be probably explained by the use of slightly different potential-energy curves and resonance widths in both LCP calculations. However, the available experiments [43–45] point to rather smaller values of the DA cross section at energies close to the DA threshold (i.e., in the region 3.7–4.5 eV), where the contribution of the $^2\Pi_g$ resonance could be significant.

The origin of the oscillatory structure in the DA cross sections is not discussed by Laporta *et al.* [18]. We propose the following explanation of its origin: The initial vibrational state is localized at larger internuclear distances than the classical
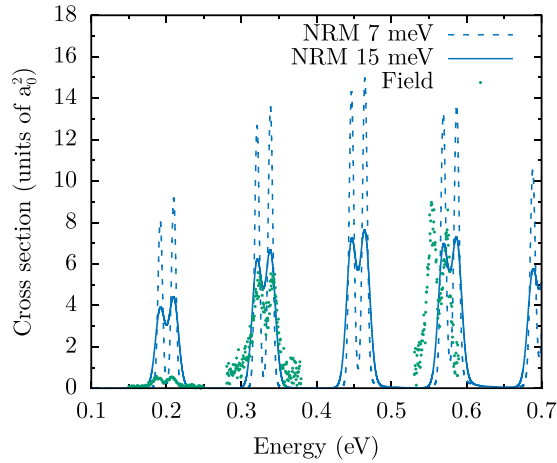
FIG. 10. Calculated resonant contribution to the total cross section obtained within our nonlocal model compared with measurements by Field *et al.* [8] (the double peak at 0.45 eV is not presented in Ref. [8]).

turning points of the anion potential-energy curve (the $^2\Pi_g$ state) at energies above the DA threshold; see $\chi_0(R)$ and large peaks of the wave functions at around $R = 2.25\ a_0$ in Fig. 14. Thus, the nuclei can move in both directions, either directly towards the DA channel or first towards the smaller internuclear distances and later, after reflection near the classical turning point, also towards the DA channel. The wave functions describing these two nuclear motions constructively interfere with each other for energies at maxima of the DA cross section. But the interference is destructive for energies at minima, giving rise to the oscillations in the DA cross sections.

V. CONCLUSION

We performed *ab initio* calculations of the $^2\Pi_g$ resonance contribution to the cross sections for vibrational excitation and dissociative attachment in collisions of electrons with
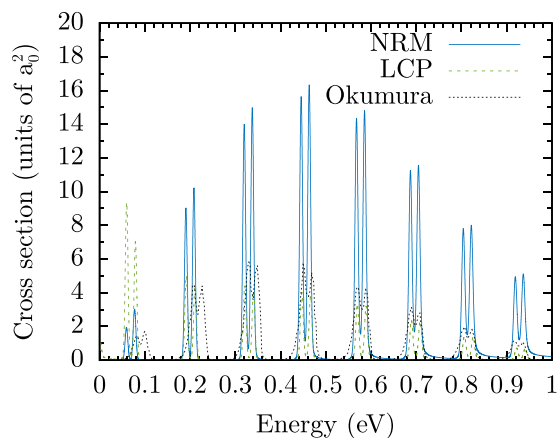

FIG. 11. Resonant contribution to the total cross sections as obtained by Okumura *et al.* [10] compared with our results calculated using the nonlocal resonance model (NRM) and the local complex potential (LCP) approximation.
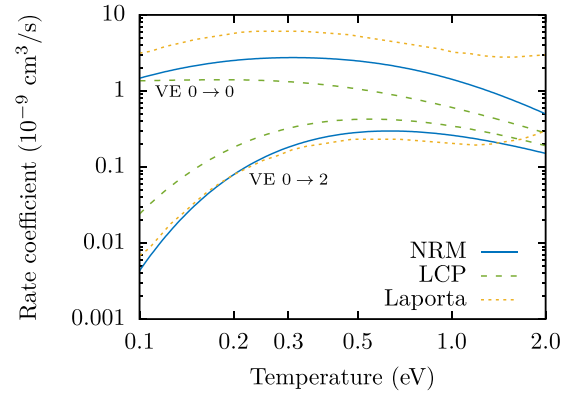

FIG. 12. Examples of sensitivity of the rate coefficients at low temperatures to the model for VE $0 \to 0$ and $0 \to 2$. Our NRM and LCP results are compared with results by Laporta *et al.* [17] also obtained within the LCP model.

O₂. Based on the fixed-nuclei data we constructed both the nonlocal resonance model and its local approximation and compared our results with available experimental and theoretical data. We included the effect of the spin-orbit interaction which leads to the separation of the peaks in the VE cross sections and better agreement with the experiments.

The overall structure of the cross sections agrees well with other works, both theoretical and experimental, and we found a good agreement in the magnitude of the spin-orbit splitting. There are, however, some discrepancies between our results and those published earlier. First, the positions of peaks are very sensitive to the relative position of the neutral and negative-ion potential-energy curves and even its small change can lead to significant differences in the cross sections. However, we estimate that the error in the positions of peaks in our results is not larger than 20–30 meV. Second, the widths of individual peaks are much smaller in our results than in other approaches. We are not sure what the reason causing this behavior is and we plan to probe this problem in more detail using a new O₂-like two-dimensional model for electron-molecule collisions similar to the models introduced
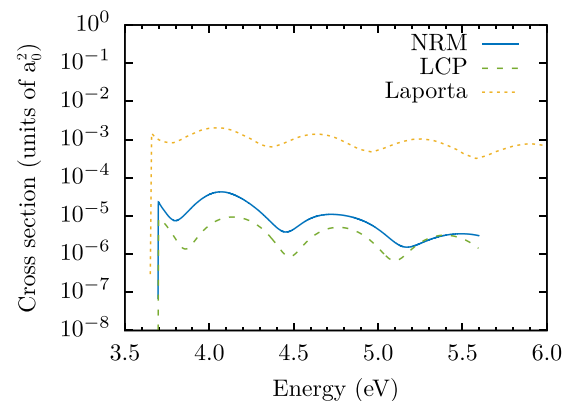

FIG. 13. Comparison of our NRM and LCP dissociative attachment cross sections for initial vibrational state $\nu_i = 0$ with the results by Laporta *et al.* [18]. Only contributions of the $^2\Pi_g$ resonance are shown.
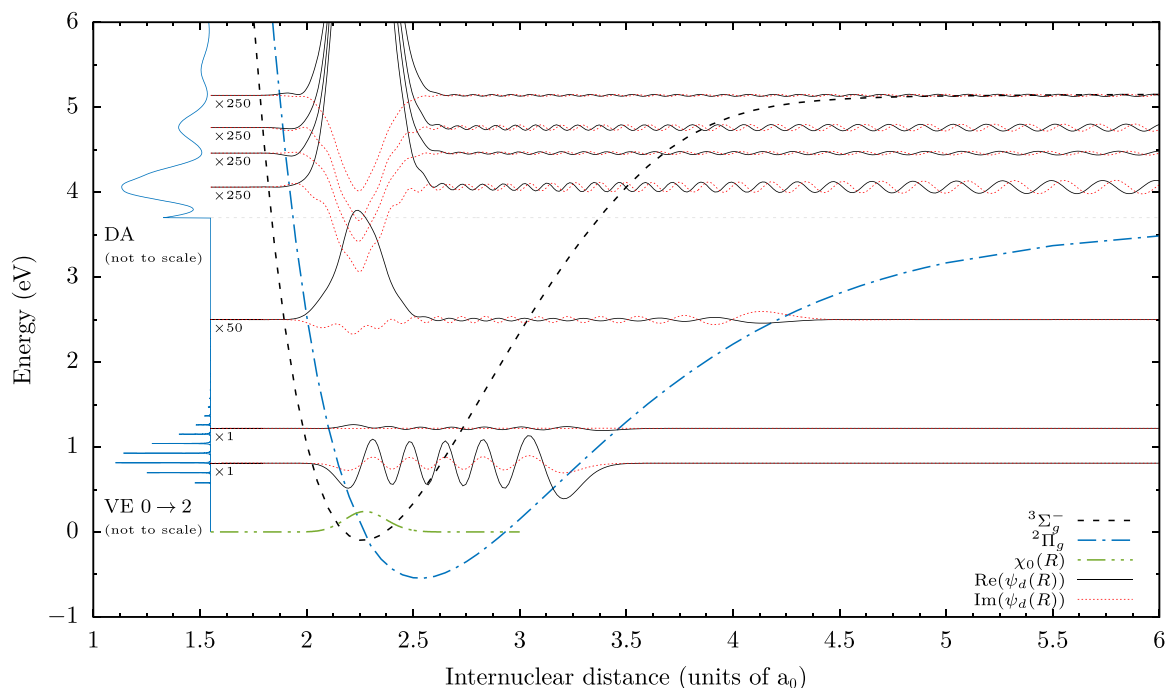
FIG. 14. Vibrational excitation $0 \rightarrow 2$ and dissociative attachment cross sections placed next to the potential-energy curves of O_2 and O_2^- together with solutions of Eq. (3) at several energies chosen to demonstrate how changes in the wave functions correspond to changes in the cross sections.

in Refs. [23,46] to compare the exact results with various approximations to nuclear dynamics used in the other works, especially with the *R*-matrix approach of Schneider *et al.* [14] which otherwise agrees with our results quite well. The direct comparison with experiments is more difficult because of the finite resolution and nonzero temperature. Our VE cross sections convolved to reproduce the specific resolution of a certain experiment are generally larger than the experimental one, but the heights of the peaks change significantly if we assume a different resolution, as shown in Fig. 10.

Finally, we should stress that large differences in the heights of the VE cross-section peaks close to the thresholds predicted by the nonlocal resonance model and its local

approximation lead to significant changes in the corresponding rate coefficients at low temperatures (as shown in Fig. 12). Therefore, the calculated rates should be used with care in applications, since it is very difficult to provide reliable data for this temperature region.

[1] L. Campbell and M. J. Brunger, Electron collisions in atmospheres, Int. Rev. Phys. Chem. **35**, 297 (2016).

[2] Y. Hatano, Y. Katsumura, and A. Mozumder, *Charged Particle and Photon Interactions with Matter: Recent Advances, Applications, and Interfaces* (CRC Press, Taylor and Francis Group, Boca Raton, 2010).

[3] A. Bultel, B. Cheron, A. Bourdon, O. Motapon, and I. Schneider, Collisional-radiative model in air for earth re-entry problems, Phys. Plasmas **13**, 043502 (2006).

[4] Y. Itikawa, Cross sections for electron collisions with oxygen molecules, J. Phys. Chem. Ref. Data **38**, 1 (2009).

[5] M. J. W. Boness and G. J. Schulz, Structure of O_2, Phys. Rev. A **2**, 2182 (1970).

[6] F. Linder and H. Schmidt, Experimental study of low energy e-O_2 collision processes, Z. Naturforsch. **26a**, 1617 (1971).

[7] J. E. Land and W. Raith, High-resolution measurement of resonances in e-O_2 scattering by electron time-of-flight spectroscopy, Phys. Rev. A **9**, 1592 (1974).

[8] D. Field, G. Mrotzek, D. W. Knight, S. Lunt, and J. P. Ziesel, High-resolution studies of electron scattering by molecular oxygen, J. Phys. B: At., Mol. Opt. Phys. **21**, 171 (1988).

[9] M. Allan, Measurement of absolute differential cross sections for vibrational excitation of O_2 by electron impact, J. Phys. B: At., Mol. Opt. Phys. **28**, 5163 (1995).

[10] T. Okumura, N. Kobayashi, A. Sayama, Y. Mori, H. Akasaka, K. Hosaka, T. Odagiri, M. Hoshino, and M. Kitajima, Total cross-section for low-energy and very low-energy electron collisions with O_2, J. Phys. B: At., Mol. Opt. Phys. **52**, 035201 (2019).

[11] C. J. Noble and P. G. Burke, R-Matrix Calculations of Low-Energy Electron Scattering by Oxygen Molecules, Phys. Rev. Lett. **68**, 2011 (1992).

[12] K. Higgins, C. J. Noble, and P. G. Burke, Low energy electron scattering by oxygen molecules, J. Phys. B: At., Mol. Opt. Phys. **27**, 3203 (1994).

[13] K. Higgins, C. J. Gillan, P. G. Burke, and C. J. Noble, Low-energy electron scattering by oxygen molecules. II. Vibrational excitation, J. Phys. B: At., Mol. Opt. Phys. **28**, 3391 (1995).

[14] B. I. Schneider, M. Le Dourneuf, and P. G. Burke, Theory of vibrational excitation and dissociative attachment: An *R*-matrix approach, J. Phys. B: At. Mol. Phys. **12**, L365 (1979).

[15] M. Tashiro, K. Morokuma, and J. Tennyson, *R*-matrix calculation of electron collisions with electronically excited O₂ molecules, Phys. Rev. A **73**, 052707 (2006).

[16] R. Naghma, M. Vinodkumar, and B. Antony, Total cross sections for O₂ and S₂ by electron impact, Radiat. Phys. Chem. **97**, 6 (2014).

[17] V. Laporta, R. Celiberto, and J. Tennyson, Resonant vibrational-excitation cross sections and rate constants for low-energy electron scattering by molecular oxygen, Plasma Sources Sci. Technol. **22**, 025001 (2013).

[18] V. Laporta, R. Celiberto, and J. Tennyson, Dissociative electron attachment and electron-impact resonant dissociation of vibrationally excited O₂ molecules, Phys. Rev. A **91**, 012701 (2015).

[19] L. Dubé and A. Herzenberg, Absolute cross sections from the "boomerang model" for resonant electron-molecule scattering, Phys. Rev. A **20**, 194 (1979).

[20] K. Houfek and M. Čížek, Applications of the nonlocal resonance theory to diatomic molecules, in *Low-Energy Electron Scattering from Molecules, Biomolecules and Surfaces*, edited by P. Čársky and R. Čurík (CRC Press, Taylor and Francis Group, Boca Raton, 2012), pp. 127–160.

[21] W. Domcke, Theory of resonance and threshold effects in electron-molecule collisions: The projection-operator approach, Phys. Rep. **208**, 97 (1991).

[22] M. Čížek and K. Houfek, Nonlocal theory of resonance electron-molecule scattering, in *Low-Energy Electron Scattering from Molecules, Biomolecules and Surfaces*, edited by P. Čársky and R. Čurík (CRC Press, Taylor and Francis Group, Boca Raton, 2012), pp. 91–126.

[23] K. Houfek, T. N. Rescigno, and C. W. McCurdy, Probing the nonlocal approximation to resonant collisions of electrons with diatomic molecules, Phys. Rev. A **77**, 012710 (2008).

[24] H. Feshbach, Unified theory of nuclear reactions, Ann. Phys. (NY) **5**, 357 (1958).

[25] H. Feshbach, A unified theory of nuclear reactions. II, Ann. Phys. (NY) **19**, 287 (1962).

[26] J. N. Bardsley, Configuration interaction in the continuum states of molecules, J. Phys. B: At. Mol. Phys. **1**, 349 (1968).

[27] P. J. Knowles and H.-J. Werner, An efficient second order MC-SCF method for long configuration expansions, Chem. Phys. Lett. **115**, 259 (1985).

[28] H.-J. Werner and P. J. Knowles, A second order MCSCF method with optimum convergence, J. Chem. Phys. **82**, 5053 (1985).

[29] P. J. Knowles and H.-J. Werner, Internally contracted multiconfiguration reference configuration interaction calculations for excited states, Theor. Chim. Acta **84**, 95 (1992).

[30] H.-J. Werner, P. J. Knowles, G. Knizia, F. R. Manby, M. Schütz, *et al.*, MOLPRO, version 2012.1, a package of *ab initio* programs (2012); see http://www.molpro.net.

[31] H.-J. Werner, P. J. Knowles, G. Knizia, F. R. Manby, and M. Schütz, Molpro: A general purpose quantum chemistry program package, Wiley Interdiscip. Rev. Comput. Mol. Sci. **2**, 242 (2012).

[32] T. H. Dunning, Gaussian basis sets for use in correlated molecular calculations. I. The atoms boron through neon and hydrogen, J. Chem. Phys. **90**, 1007 (1989).

[33] D. Lide, *CRC Handbook of Chemistry and Physics: A Ready-Reference Book of Chemical and Physical Data* (CRC Press, Boca Raton, 2009) .

[34] J. Tennyson, Electron–molecule collision calculations using the *R*-matrix method, Phys. Rep. **491**, 29 (2010).

[35] J. M. Carr, P. G. Galiatsatos, J. D. Gorfinkiel, A. G. Harvey, M. A. Lysaght, D. Madden, Z. Masin, M. Plummer, J. Tennyson, and H. N. Varambhia, UKRmol: A low-energy electron- and positron-molecule scattering suite, Eur. Phys. J. D **66**, 58 (2012).

[36] Z. Mašín, J. Benda, J. D. Gorfinkiel, A. G. Harvey, and J. Tennyson, UKRmol+: A suite for modelling electronic processes in molecules interacting with electrons, positrons and photons using the R-matrix method, Comput. Phys. Commun. **249**, 107092 (2020).

[37] J. Tennyson and C. J. Noble, Reson—A program for the detection and fitting of Breit-Wigner resonances, Comput. Phys. Commun. **33**, 421 (1984).

[38] G. V. Mil'nikov, H. Nakamura, and J. Horáček, Stable and efficient evaluation of Green's function in scattering problem, Comput. Phys. Commun. **135**, 278 (2001).

[39] K. Houfek, M. Čížek, and J. Horáček, Dissociative attachment of low-energy electrons to vibrationally excited hydrogen molecules, Czech. J. Phys. B **52**, 29 (2002).

[40] J. A. Nelder and R. Mead, A simplex method for function minimization, Comput. J. **7**, 308 (1965).

[41] G. Parlant and F. Fiquet-Fayard, The O₂-²Π*g* resonance: theoretical analysis of electron scattering data, J. Phys. B: At. Mol. Phys. **9**, 1617 (2001).

[42] I. Levine, *Quantum Chemistry* (Pearson, Boston, 2014).

[43] G. J. Schulz, Cross sections and electron affinity for O⁻ ions from O₂, CO, and CO₂ by electron impact, Phys. Rev. **128**, 178 (1962).

[44] D. Rapp and D. D. Briglia, Total cross sections for ionization and attachment in gases by electron impact. II. Negative-ion formation, J. Chem. Phys. **43**, 1480 (1965).

[45] L. G. Christophorou, R. N. Compton, G. S. Hurst, and P. W. Reinhardt, Determination of electron-capture cross sections with swarm-beam techniques, J. Chem. Phys. **43**, 4273 (1965).

[46] K. Houfek, T. N. Rescigno, and C. W. McCurdy, Numerically solvable model for resonant collisions of electrons with diatomic molecules, Phys. Rev. A **73**, 032721 (2006).